

## Characterization of the $3d\delta$ Rydberg state of $\text{MgAr}^+$ using a quantum-control optical scheme

M. Génévriez , D. Wehrli , T. Berglitsch , and F. Merkt \*

Laboratory of Physical Chemistry, ETH Zürich, CH-8093 Zürich, Switzerland

 (Received 15 June 2021; accepted 16 July 2021; published 18 October 2021)

We report a spectroscopic investigation of the  $3d\delta_\Omega$  ( $\Omega = \frac{3}{2}, \frac{5}{2}$ ) Rydberg states of the  $\text{MgAr}^+$  molecular cation. Vibrational levels of the  $3d\delta_{3/2}$  spin-orbit component with  $v \geq 15$  were observed to directly predissociate into charge-transfer continua correlating to the  $\text{Mg}(3s^2\ ^1S) + \text{Ar}^+(3p^5\ ^2P)$  dissociation limit, making it possible to record their spectra by isolated-core multiphoton Rydberg dissociation spectroscopy. Vibrational states below  $v = 15$ , which do not predissociate, were characterized with partial rotational resolution using a multiphoton excitation and dissociation quantum-control scheme that radiatively couples the  $3d\delta$  vibronic states to predissociative levels of the  $3d\pi$  state. An effective Hamiltonian approach was used to theoretically investigate this scheme, including the origin of the control over the spectral lineshapes provided by the laser detuning. This approach provided results in quantitative agreement with the measured spectra. Potential-energy functions were derived for the  $3d\delta_\Omega$  states from experimental data. They are very similar to the one of the  $X^{2+}\ ^1\Sigma^+$  ground state of the  $\text{MgAr}^{2+}$  doubly charged ion, highlighting the Rydberg character of the  $3d\delta$  state. Whereas homogeneous charge-transfer interactions play a major role in the dynamics of the Rydberg states of molecular ions, the present study shows that heterogeneous interactions leave these states essentially unaffected.

DOI: [10.1103/PhysRevA.104.042811](https://doi.org/10.1103/PhysRevA.104.042811)

### I. INTRODUCTION

Little is known concerning the Rydberg states of positively charged molecular ions, in contrast with the extensive data available for the Rydberg states of neutral molecules (see, e.g., Refs. [1–6] and references therein). In addition to their interest for high-resolution photoelectron spectroscopy [7–10], the Rydberg states of molecular ions act as transient resonances in ion-neutral collisions [11–14]. Recent efforts have been directed toward the systematic investigation and characterization of the low- and high-lying Rydberg states of the  $\text{MgAr}^+$  molecular ion [10,15–17]. These efforts are motivated by the fact that  $\text{MgAr}^{2+}$  is so far the only thermodynamically stable doubly charged ion that has been characterized by high-resolution spectroscopy [10]. Its thermodynamical stability implies the existence of sharp Rydberg series in  $\text{MgAr}^+$ . Systematic investigations of these series open up the prospect of the first extensive characterization of the Rydberg states of a molecular cation.

The low-lying  $3p$  Rydberg complex [15,16] and the  $3d\pi$  state belonging to the  $3d$  complex [17] of  $\text{MgAr}^+$  were characterized by isolated-core multiphoton Rydberg dissociation (ICMRD) spectroscopy [18]. This method is analogous to resonance-enhanced multiphoton dissociation (REMPD) spectroscopy [19,20] but for the ion core of a Rydberg molecule. In the region of the  $3d$  and  $4s$  complexes, located about  $70\,000\text{ cm}^{-1}$  above the electronic ground state of  $\text{MgAr}^+$ , the electronic states associated to the  $\text{Mg}^+(4s\ ^2S_{1/2}, 3d\ ^2D_{3/2,5/2}) + \text{Ar}(3p^6\ ^1S_0)$  and  $\text{Mg}(3s^2\ ^1S_0) + \text{Ar}^+(3p^5\ ^2P_{1/2,3/2})$  dissociation thresholds overlap spectrally,

as shown in Fig. 1 (see also Fig. 2 in Ref. [17]). The potential-energy functions of these five groups of states cross and this energy region represents a prototypical example of the major role played by charge-transfer nonadiabatic interactions in the dynamics of the Rydberg states of molecular ions [17]. The  $3d\pi_\Omega$  Rydberg states studied in Ref. [17] possess the same electronic symmetry as the charge-transfer states ( $^2\Pi_{1/2,3/2}$ ) and homogeneous interactions cause the rapid decay of most of their vibrational levels by predissociation, which can happen on the sub-ps timescale. The  $3d\delta_\Omega$  states, on the other hand, possess different electronic symmetries ( $^2\Delta_{3/2,5/2}$ ), allowing one to study whether and, if so, how *heterogeneous* charge-transfer interactions affect the structure and dynamics of the Rydberg states of molecular ions.

A major difficulty encountered in the course of this study is that nonpredissociative levels of the  $3d\delta_\Omega$  Rydberg states cannot be studied by ICMRD and REMPD because they cannot be efficiently dissociated. Photoionization of these nonpredissociative levels of  $\text{MgAr}^+$  to the  $\text{MgAr}^{2+}$  doubly charged ion did not produce any observable signal, such that resonance-enhanced multiphoton ionization spectra could not be recorded either. The development of an alternative technique was therefore required that is sensitive enough to record high-resolution spectra despite the low density of the ion sample (e.g.,  $\approx 10^4\text{ cm}^{-3}$  for  $\text{MgAr}^+$  molecules in their ground electronic state [10]).

We describe in this article a highly sensitive method based on a double-resonance spectroscopy scheme involving the  $3d\delta$  state and a dissociation continuum. Multiphoton double-resonance schemes involving dissociation continua have been developed [21–26] in the context of quantum control of molecular reactions [27–30], with the goal to steer the reaction dynamics into specific product channels. The properties of the

\*merkt@phys.chem.ethz.ch

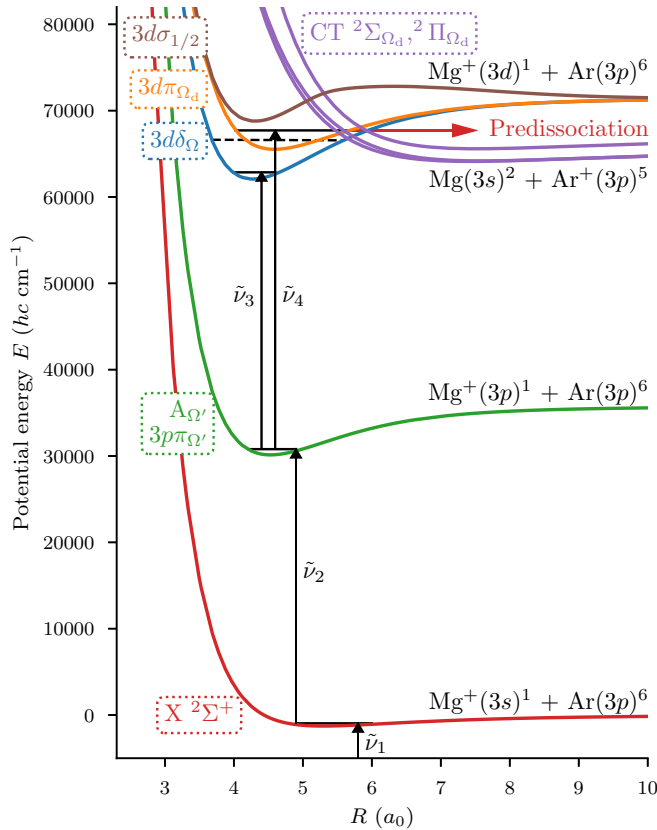


FIG. 1. Excitation scheme used to study the  $3d\delta_{\Omega}$  Rydberg states of  $\text{MgAr}^+$  and relevant potential-energy functions. The curves of the  $X$ ,  $A$ ,  $3d\sigma$ ,  $3d\pi$ , and  $3d\delta$  states are *ab initio* data taken from Ref. [15] and the curves of the charge-transfer (CT) states were taken from Ref. [17]. The red horizontal arrow indicates predissociation of  $3d\pi$  vibrational levels into the continua associated with the CT states. The horizontal black dashed line indicates the position of the  $3d\delta_{3/2}(v = 15)$  vibrational level.

laser light used, e.g., its phase or frequency, act as control parameters. Coherent and incoherent control schemes, including stimulated Raman adiabatic passage (STIRAP) [31,32], wavepacket design [21,33], or pulse-shaping techniques based on optimal control theory [29,34,35], have been applied to a variety of molecules and solid-state systems (see, e.g., Refs. [27–29,36,37] and references therein).

The scheme used in the present work is inspired from incoherent manipulation schemes developed in Refs. [22,23,38,39], which achieve control by tailoring the quantum interferences between different photoexcitation and photodissociation pathways. These schemes permitted, for example, the modification of branching ratios between different dissociation channels of  $\text{Na}_2$  by tuning the photon energy of a “control” laser beam [22]. Aside from chemical-reaction control, quantum interferences between different multiphoton-dissociation pathways encode, in the dissociation spectra, spectroscopic information on the states involved. As in quantum-control approaches, such interferences can be designed to make spectroscopic data easily accessible from the experimental spectra. We demonstrate that quantum-control schemes are powerful tools

to carry out high-resolution spectroscopic investigations of electronically excited states of molecular ions that remain otherwise unobservable by action-spectroscopy methods such as ICMRD or REMPD.

We present a study of the vibrational and rotational structure of the two spin-orbit components of the  $3d\delta$  electronic state of  $\text{MgAr}^+$ . Vibrational levels of the  $3d\delta_{3/2}$  state with  $v \geq 15$  were observed to directly predissociate into charge-transfer continua correlating to the  $\text{Mg}(3s^2\ ^1S) + \text{Ar}^+(3p^5\ ^2P)$  dissociation limit, and their spectra were recorded with partial rotational resolution using ICMRD. Vibrational levels of the  $3d\delta_{3/2}$  and  $3d\delta_{5/2}$  states with  $v \leq 14$  did not predissociate. They were recorded using a multiphoton excitation and dissociation quantum-control scheme which radiatively coupled the predissociative  $3d\pi$  state, acting as a dissociation continuum, with the nonpredissociative levels of the  $3d\delta$  state we wish to study. The experimental setup and excitation scheme are presented in Sec. II. Anticipating on the results, the lines we recorded for the vibrational levels with  $v \leq 14$  were found to be asymmetric and their shapes strongly depended on the laser detunings. In order to understand this behavior and assign the spectra, we developed a time-dependent effective-Hamiltonian approach to model the excitation and dissociation dynamics and calculate the experimental spectra, as described in Sec. III. The experimental and theoretical results are presented and compared in Sec. IV. The spectra we recorded for  $v \leq 14$  are presented in Sec. IV A and the origin of their asymmetry and dependence on the laser detunings is discussed and attributed to quantum interferences between two multiphoton-dissociation pathways based on a simple Fano-type model [40]. The quantitative analysis of the spectra and their assignment using the effective Hamiltonian approach of Sec. III is reported in Sec. IV B. The spectra of the  $3d\delta_{3/2}(v \geq 15)$  vibrational levels recorded by ICMRD and their analysis are discussed in Sec. IV C. The results comprise the positions and rotational constants of 36 vibrational levels belonging to the two spin-orbit components of the  $3d\delta$  state ( $\Omega = \frac{3}{2}$  and  $\frac{5}{2}$ ) of  $\text{MgAr}^+$ . The analysis led to the spectroscopic characterization of these states, for which we derive accurate molecular constants (Sec. IV D) and potential-energy functions (Sec. IV E). The quantum-control technique we used to measure vibrational levels of the  $3d\delta$  state that cannot be efficiently dissociated is applicable to other molecules, and works regardless of whether a Rydberg electron is present. It opens up a way to study excited states of molecular ions that cannot be investigated by REMPD, ICMRD, or other action-spectroscopy schemes.

## II. EXPERIMENT

The experimental setup is described in detail elsewhere [9,41]. Briefly,  $\text{MgAr}$  molecules are formed predominantly in their a  $^3\Pi_0$  metastable state by laser ablation of a Mg rod with the second harmonic of a pulsed Nd:YAG laser. Ablation occurs within the nozzle of a pulsed supersonic-expansion source, using Ar as carrier gas. Molecules are cooled in the expansion to rotational temperatures of  $\approx 3$  K [41]. After passing through a 3-mm-diameter skimmer located 8 cm downstream from the nozzle, the molecules enter the photoexcitation chamber. The molecular beam is intersected at right angles by

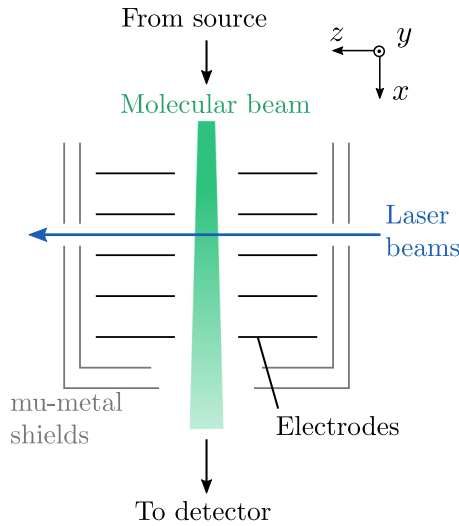


FIG. 2. Schematic view of the photoexcitation region. The molecular beam produced by the laser ablation supersonic expansion source enters the electrode stack (horizontal full lines) from the top and is intersected at right angles by up to four laser beams. Pulsed electric fields are applied to the electrodes to field ionize atoms and molecules in Rydberg states and to accelerate the positively charged particles toward the detector located  $\approx 15$  cm below the interaction region. The reference frame used in Sec. III is defined in the top right corner of the figure.

up to four copropagating pulsed laser beams (pulse duration  $\approx 5$  ns, repetition rate 25 Hz) from four dye lasers pumped by the second harmonic of a seeded  $Q$ -switched Nd:YAG laser. The fundamental outputs of these dye lasers are frequency doubled or frequency tripled with nonlinear crystals. Their wave numbers are measured using a commercial wavemeter with a stated accuracy of  $0.02 \text{ cm}^{-1}$  and their bandwidths are of the order of  $0.1 \text{ cm}^{-1}$ . The laser beams enter the vacuum chamber through an uncoated window and leave it through a window at Brewster's angle, after which the pulse energies are measured with a pyroelectric pulse-energy meter.

The interaction between the molecules and the laser light occurs within a 5.8-cm-long stack of five resistively coupled cylindrical electrodes (see Fig. 2). Two concentric mu-metal shields surround the stack to suppress stray magnetic fields. The electrodes serve to apply pulsed electric fields in the photoexcitation region in order to field ionize molecules and atoms in Rydberg states. The applied pulsed fields also extract all positively charged particles into a linear time-of-flight (TOF) tube at the end of which they are detected by a microchannel-plate detector.

The excitation scheme used to study the two spin-orbit components of the  $3d\delta_{\Omega}$  ( $\Omega = \frac{3}{2}, \frac{5}{2}$ ) state of  $\text{MgAr}^+$  is shown in Fig. 1. Neutral molecules are excited with a first laser with wave number  $\tilde{\nu}_1$  to a high Rydberg state (principal quantum number  $n \approx 130$ ) belonging to a series converging to a specific vibrational level  $v''$  of the ground electronic state of the molecular ion. After 10 ns, pulsed radiation from three other lasers resonantly excites and dissociates the ion core of the Rydberg molecule by ICMRD. We verified in previous work that the ion core dissociation process is identical to that in the bare molecular ion at sufficiently high  $n$  values

(i.e.,  $n > 100$ ) [18]. The second laser with wave number  $\tilde{\nu}_2$  resonantly or near resonantly drives the transition from the selected vibrational level of the ground electronic state  $X(v'')$  to a vibrational level of one of the two spin-orbit components ( $\Omega' = \frac{1}{2}, \frac{3}{2}$ ) of the first electronically excited state,  $A_{\Omega'}(v')$ . The third laser ( $\tilde{\nu}_3$ ) couples the  $A_{\Omega'}(v')$  state to a vibrational level  $v$  of one of the two spin-orbit components of the  $3d\delta$  state. The fourth laser ( $\tilde{\nu}_4$ ) couples the  $A_{\Omega'}(v')$  state to a vibrational level  $v_d$  of the  $3d\pi_{\Omega_d}$  ( $\Omega_d = \frac{1}{2}, \frac{3}{2}$ ) states. For  $v_d \geq 6$  ( $\Omega_d = \frac{1}{2}$ ) and  $v_d \geq 5$  ( $\Omega_d = \frac{3}{2}$ ), the vibrational levels rapidly predissociate into the continua of the three charge-transfer (CT) states correlating, in the separated-atom limit, to  $\text{Ar}^+(3p^5 \ ^2P_{1/2,3/2}) + \text{Mg}(3s^2 \ ^1S_0)$ . This process was investigated in detail in Ref. [17]. Upon dissociation of the ion core, the Rydberg electron follows the charged fragment, yielding an Ar atom in a high- $n$  Rydberg state [17,18]. In the experiment, these atoms are selectively detected by delayed pulsed-field ionization and TOF mass spectrometry, which permits the background-free monitoring of the predissociation events through the detection of  $\text{Ar}^+$  (see Ref. [18] for details). Spectra are recorded by monitoring the  $\text{Ar}^+$  signal as a function of the wave number  $\tilde{\nu}_3$  of laser 3.

All spectra presented below are for the most abundant  $^{24}\text{Mg}^{40}\text{Ar}$  isotope (natural abundances:  $^{24}\text{Mg}$  (79%),  $^{25}\text{Mg}$  (10%),  $^{26}\text{Mg}$  (11%),  $^{36}\text{Ar}$  (0.34%),  $^{38}\text{Ar}$  (0.06%), and  $^{40}\text{Ar}$  (99.60%), respectively [42]). The assignment of the vibrational levels of the  $3d\delta_{\Omega}$  states to specific vibrational quantum numbers  $v$  could not be determined from an isotopic-shift analysis [43] because the signal for  $^{25}\text{MgAr}$  and  $^{26}\text{MgAr}$  was too low. The present attribution is based on the facts that (i) no line could be measured below the level we assigned to  $v = 0$  and (ii) the Franck-Condon factors calculated from the potential-energy functions shown in Fig. 1 are in good agreement with the relative intensities of the measured vibrational bands. This assignment is in agreement with the predictions of the *ab initio* calculations presented in Ref. [15], which also agreed with the assignment we derived from isotopic-shift analyses for the  $X$ ,  $A$ , and  $3d\pi$  states [16,17,41].

### III. THEORY

The experimental spectra of the vibrational levels  $v \leq 14$  of the  $3d\delta$  state recorded using the excitation scheme shown in Fig. 1 exhibit asymmetric lines, with profiles strongly dependent on the wave number  $\tilde{\nu}_2$  of the second laser (see Sec. IV). Consequently, a direct assignment and analysis of the spectra to extract vibrational-level positions and rotational constants is not possible. In order to quantitatively calculate, assign, and analyze the spectra, we developed a nonperturbative effective-Hamiltonian approach describing the excitation and dissociation dynamics of the  $\text{MgAr}^+$  ion core. It explicitly includes all resonant and near-resonant states and reproduces the experimental conditions as closely as possible. Excitation of the neutral  $\text{MgAr}$  molecules in the  $a^3\Pi_0(v=0, J)$  states to high- $n$  Rydberg states with a  $\text{MgAr}^+$  core in the selected  $X(v'')$  state occurs 10 ns before excitation and dissociation of the ion core. This step is therefore not considered explicitly in the model. Atomic units are used throughout this section.

The effective Hamiltonian describing the resonant and near-resonant excitation and predissociation dynamics

occurring in the ion core can be written, in the rotating-wave approximation and after adiabatic elimination of the continua [44], as

$$H_{\text{eff}}(t) = \begin{pmatrix} H_X & \frac{1}{2}\Omega_{X-A}^*(t) & 0 & 0 \\ \frac{1}{2}\Omega_{X-A}(t) & H_A & \frac{1}{2}\Omega_{A-3d\delta}^*(t) & \frac{1}{2}\Omega_{A-3d\pi}^*(t) \\ 0 & \frac{1}{2}\Omega_{A-3d\delta}(t) & H_{3d\delta} & 0 \\ 0 & \frac{1}{2}\Omega_{A-3d\pi}(t) & 0 & H_{3d\pi} \end{pmatrix}. \quad (1)$$

In the above equation, the terms  $H_\alpha$  denote the Hamiltonians describing the laser fields and the molecule in a given electronic state  $\alpha$ , without interaction between the two. Each term is written as a matrix that includes all the relevant near-resonant rovibrational states. The matrices  $\Omega_{\alpha-\alpha'}$  contain the Rabi frequencies of the near-resonant rovibronic transitions between the electronic states  $\alpha$  and  $\alpha'$ . Their time dependence reflects the time dependence of the laser intensities.

We use a basis of molecular eigenstates in the Born-Oppenheimer approximation. Consequently, the terms along the diagonal in Eq. (1) represent diagonal matrices, the elements of which are calculated from the experimental term values and rotational constants of the  $X$ ,  $A$ , and  $3d\pi$  states [16,17,41], and also from the experimental predissociation widths of the  $3d\pi$  state [17]. The term values and rotational constants for the  $3d\delta$  state were extracted from the experimental spectra, as described in Sec. IV B. The  $X \ ^2\Sigma^+$  state is well described by Hund's angular-momentum coupling case (b), thus [45,46]

$$\begin{aligned} \langle X, v''N''J''M''_J | H_X | X, v''N''J''M''_J \rangle \\ = T_{v''}^X + B_{v''}^X N''(N'' + 1), \end{aligned} \quad (2)$$

where  $N''$ ,  $J''$ , and  $M''_J$  are the quantum numbers for the angular momentum without spin, the total angular momentum and its projection onto the laboratory-fixed-frame quantization axis, respectively.  $B_{v''}$  is the rotational constant of the vibrational state and  $T_{v''}$  is its vibronic term value. The  $A$ ,  $3d\pi$ , and  $3d\delta$  states are well described by Hund's angular momentum coupling case (a) in the range of vibrational levels probed in the experiment, and their term symbols are  $^2\Pi_{\Omega'}$ ,  $^2\Pi_{\Omega_d}$ , and  $^2\Delta_{\Omega}$ , respectively, with  $\Omega' = \Omega_d = \frac{1}{2}, \frac{3}{2}$  and  $\Omega = \frac{3}{2}, \frac{5}{2}$ . The diagonal elements of the  $H_\alpha$  matrices for these states are given by the general expression [45,46]

$$\begin{aligned} \langle \alpha, v\Omega JM_J | H_\alpha | \alpha, v\Omega JM_J \rangle \\ = T_v^\alpha + B_v^\alpha [J(J+1) - \Omega^2] - i \frac{\Gamma_v^\alpha}{2} - \sum_i \omega_i, \end{aligned} \quad (3)$$

where  $\Gamma_v^\alpha$  is the predissociation width of the vibronic state and is only nonzero for vibrational levels of the  $3d\pi_{\Omega_d}$  states with  $v_d \geq 6$  for  $\Omega_d = \frac{1}{2}$  and  $v_d \geq 5$  for  $\Omega_d = \frac{3}{2}$  [17]. The sum over the photon angular frequencies  $\omega_i$  includes the frequency of laser 2 for the  $A$  state, those of lasers 2 and 3 for the  $3d\delta$  state and those of lasers 2 and 4 for the  $3d\pi$  state, respectively (see Fig. 1).

The Rabi frequencies of the rovibronic transitions are calculated from the electric-dipole transition moments using the

general expression

$$\begin{aligned} \langle \alpha', v'\Omega'J'M'_J | \Omega_{\alpha-\alpha'}(t) | \alpha, v\Omega JM_J \rangle \\ = -\sqrt{I_i(t)} D_{\alpha,\Omega JM_J}^{\alpha',\Omega'J'M'_J} \int dR \chi_{v'}^{\alpha'}(R)^* \mu_{\text{el}}^{\alpha-\alpha'}(R) \chi_v^\alpha(R), \end{aligned} \quad (4)$$

where  $I_i(t)$  is the intensity of the  $i$ th laser driving the transition under consideration and  $D_{\alpha,\Omega JM_J}^{\alpha',\Omega'J'M'_J}$  is the angular part of the transition dipole moment, which can be calculated analytically using Hund's coupling case (a) and Hund's coupling case (b) rotational wave functions [45,46]. The notation in the above equation is for Hund's coupling case (a) states but can be straightforwardly adapted when the initial or final state is described by Hund's coupling case (b). In the experiment, the polarizations of lasers 2–4 were linear and parallel to each other. Consequently, the selection rule  $\Delta M_J = 0$  applies. The three terms in the integral on the right-hand side of Eq. (4) are the vibrational wave function of the final state, the electronic transition dipole moment, and the vibrational wave function of the initial state, respectively.  $R$  represents the internuclear distance.

We assume that  $\mu_{\text{el}}^{\alpha-\alpha'}(R)$  is  $R$  independent and that its value is close to the corresponding transition of the isolated  $\text{Mg}^+$  atomic ion. This assumption is justified by the fact that, in  $\text{MgAr}^+$ , one of the predominant binding interactions is the electrostatic charge induced dipole interaction between the  $\text{Mg}^+$  ion and the Ar atom [16,41,47] such that, to a reasonable approximation, the  $\text{Mg}^+$  ion can be considered as isolated. The  $X$ - $A$ ,  $A$ - $3d\pi$ , and  $A$ - $3d\delta$  electronic transition moments are set equal to the transition moments of the atomic transitions  $3s(m_l = 0) - 3p(m_l = 1)$ ,  $3p(m_l = 1) - 3d(m_l = 1)$ , and  $3p(m_l = 1) - 3d(m_l = 2)$ , respectively. The atomic electronic transition moments are calculated from one-electron spin orbitals of  $\text{Mg}^+$  obtained by solving the one-electron Schrödinger equation for a model potential describing the  $\text{Mg}^{2+}$  closed-shell core using a Legendre-Gauss-Lobatto discrete variable representation (DVR) method (see Ref. [48] for details). These values were later adjusted to visually match the overall shape of the experimental spectra, and an optimum was found when scaling all three atomic electronic transition moments by  $\frac{2}{3}$ . The vibrational wave functions in Eq. (4) are calculated by solving the nuclear Schrödinger equation with the potential-energy functions from Refs. [15,16,41] using the same DVR method.

All laser beams are modeled by a Gaussian time envelope with a full width at half maximum (FWHM)  $\tau = 5$  ns, matching the experimental pulse profiles recorded with a fast photodiode, and a Gaussian spatial profile with a waist  $w_0 = 0.5$  mm which we measured previously [9]. Because the laser beams are unfocused, their divergence across the interaction volume with the molecules is neglected. We write the intensity  $I_i$  of the  $i$ th laser as

$$I_i(r, t) = \frac{2E_i}{\tau\pi w_0^2} e^{-2r^2/w_0^2} e^{-4 \ln 2 \frac{t^2}{\tau^2}}, \quad (5)$$

where  $r$  is the radial distance from the beam center in a plane perpendicular to the direction of propagation ( $z$ ) of the laser beams. The molecular-beam axis is along the  $x$  direction and the laser-polarization axis along the  $y$  direction (see Fig. 2).  $E_i$  is the pulse energy. The three lasers beams reach their

peak intensity at the geometric center of the molecular beam at  $t = 0$ .

The time-dependent Schrödinger equation for the effective Hamiltonian  $H_{\text{eff}}(t)$  is solved iteratively using

$$|\psi(t + \Delta t)\rangle = e^{-iH_{\text{eff}}(t)\Delta t} |\psi(t)\rangle, \quad (6)$$

where the matrix exponential is calculated numerically [49]. The propagation time step  $\Delta t = 10^{-10}$  s was chosen to ensure that the calculations are well converged. The propagation starts at  $t_i = -10$  ns, corresponding to the time when the first laser excites the neutral molecules to a Rydberg state, and runs for 20 ns. Because of the finite predissociation widths of the vibrational levels of the  $3d\pi_{\Omega_d}$  states, the norm of the wave function decreases during the time propagation. The dissociation yield is computed at the end of the propagation ( $t_f = 10$  ns) as

$$N_d = 1 - |\langle \psi(t_f) | \psi(t_f) \rangle|^2. \quad (7)$$

The time propagation and calculation of the dissociation yield are repeated at a number of radial positions  $r$ , which correspond to different laser peak intensities [see Eq. (5)].

The total dissociation yield  $N_{\text{tot}}$ , averaged over the interaction volume, is then calculated using

$$N_{\text{tot}} = \int_0^\infty \int_{-\infty}^{+\infty} 2\pi dr dz r n_{\text{MgAr}^+}(r, z) N_d(r), \quad (8)$$

where  $n_{\text{MgAr}^+}(r, z)$  is the initial density distribution of MgAr molecules in  $[X(v'')n]$  Rydberg states, which are produced by photoexcitation of metastable MgAr molecules by the first laser pulse. Assuming that the density of metastable MgAr is uniform within the molecular beam,  $n_{\text{MgAr}^+}(r, z)$  is given by a Gaussian function along the  $r$  direction ( $w_0 = 0.5$  mm) and is uniform along the  $z$  direction for  $z$  values lying within the molecular-beam diameter ( $|z| \leq 1$  cm). The motion of the molecules across the interaction volume during the  $\approx 5$ -ns-long interaction time is negligible.

Because the Rydberg-excitation step (with laser 1) does not select specific rotational levels, the initial rotational states of the selected  $X(v'')$  vibronic state are assumed to be thermally distributed. We also assume that the ionic cores are randomly oriented in space; i.e., all  $M''$  values are equiprobable. Such assumptions were shown to represent a good approximation of the initial-state distribution in previous work [18]. The time propagation is performed for each initial rotational state, starting at time  $t_i$ , with

$$|\psi(t_i)\rangle = |X, v''N''J''M''\rangle. \quad (9)$$

The individual total dissociation yields  $N_{\text{tot}}$  are then incoherently summed with weights given by the initial-state distribution. Finally, the entire procedure is repeated for different values of the wave number  $\tilde{\nu}_3$  of laser 3 to calculate the spectra we recorded experimentally. The theoretical spectra are convoluted by a Gaussian function with a full width at half maximum of  $0.2 \text{ cm}^{-1}$  to account for the effect of the laser bandwidth.

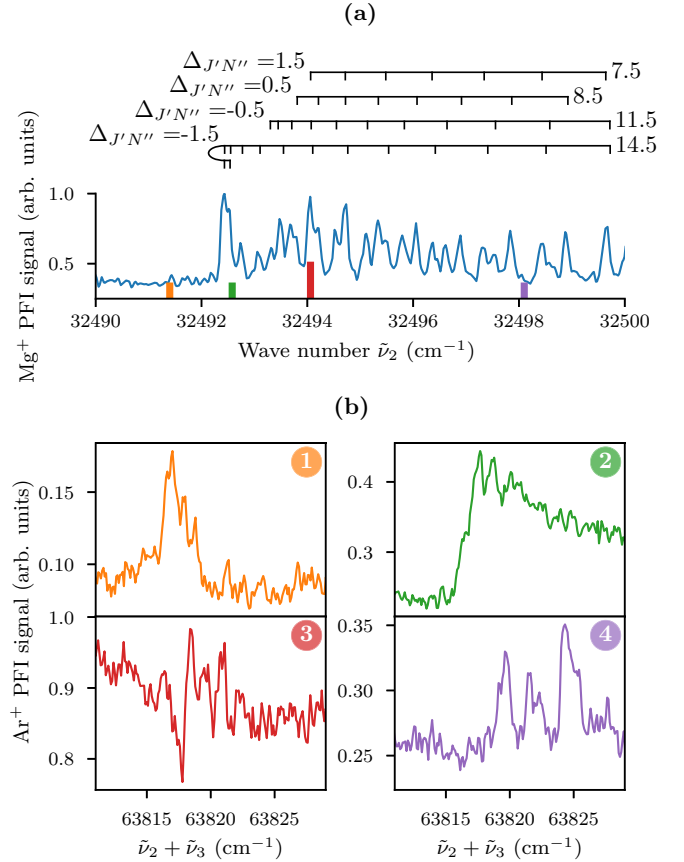


FIG. 3. Spectra of (a) the  $A_{3/2}(v' = 5) \leftarrow X(v'' = 3)$  transition of MgAr $^+$  recorded by ICMRD (see Refs. [16,18] for details) and (b) the  $3d\delta_{5/2}(v = 2) \leftarrow X(v'' = 3)$  two-photon transition for different wave numbers  $\tilde{\nu}_2$  of the second laser corresponding to the vertical colored bars in panel (a), which match the colors and numbering of the spectra in panel (b) [graphs 1–4 match the bars from left to right in panel (a)].

## IV. RESULTS AND DISCUSSION

### A. Experimental spectra of the $3d\delta_{\Omega}(v \leq 14)$ levels and qualitative interpretation

Spectra of the  $3d\delta_{5/2}(v = 2) \leftarrow X(v'' = 3)$  two-photon transition recorded by monitoring the Ar $^+$  predissociation signal as a function of  $\tilde{\nu}_3$  are shown in Fig. 3(b) for different laser 2 wave numbers  $\tilde{\nu}_2$ . The assignment of the spectra to  $\Omega = \frac{5}{2}$  is based on the fact that (i) laser 2 is resonant or near resonant with the  $A_{3/2}(v' = 5) \leftarrow X(v'' = 3)$  transition and (ii) electric-dipole selection rules for transitions between two states described by Hund's case (a) require that  $\Delta\Lambda = \Delta\Omega$ , which implies that  $\Omega = \Omega' + 1$  for a transition from a  $\Pi$  to a  $\Delta$  state. The wave numbers  $\tilde{\nu}_2$  were set at 32491.40, 32492.58, 32494.06, and 32498.10  $\text{cm}^{-1}$  for the spectra labeled 1–4, respectively, and these positions are marked in the spectrum of the  $A_{3/2}(v' = 5) \leftarrow X(v'' = 3)$  transition by the vertical bars [Fig. 3(a)]. They correspond to different detunings with respect to the intermediate rovibronic transitions. The spectra in Fig. 3(b) reveal the strong influence  $\tilde{\nu}_2$  has on the spectral profiles.

We first consider excitation at  $32\,494.06\text{ cm}^{-1}$  [panel 3 in Fig. 3(b)], which follows the behavior expected for double-resonance spectroscopy between bound states. Laser 2 is resonant with a few rovibronic transitions and transfers population from the initial  $X(v'' = 3)$  state to the intermediate  $A_{3/2}(v' = 5)$  state. The population in the intermediate state is drained by laser 4 ( $\tilde{\nu}_4 = 35\,500.08\text{ cm}^{-1}$ ), which resonantly excites molecules from the  $A_{3/2}(v' = 5)$  state to the predissociative  $3d\pi_{3/2}(v_d = 6)$  state with  $\Gamma_6^{3d\pi_{3/2}} = 18(4)\text{ cm}^{-1}$  [17]. When the wave number of laser 3 is resonant with a transition to rovibronic levels of the  $3d\delta_{5/2}$  state, some population is transferred to this state instead. Because the  $3d\delta_{5/2}(v)$  states with  $v \leq 14$  do not predissociate into  $\text{Ar}^+ + \text{Mg}$ , the overall  $\text{Ar}^+$  predissociation signal drops, as observed in panel 3 of Fig. 3(b). The dips in the spectrum thus lie at the positions of  $3d\delta_{5/2}(v = 2, J) \leftarrow A_{3/2}(v' = 5, J') \leftarrow X(v'' = 3, N'')$  two-photon transitions.

The spectral profiles recorded when laser 2 is off resonance are less obvious to interpret. At the  $\tilde{\nu}_2$  values of  $32\,491.40\text{ cm}^{-1}$  and  $32\,498.10\text{ cm}^{-1}$  (panels 1 and 4 in Fig. 3(b), respectively), a large *increase* of the predissociation signal is observed when the sum  $\tilde{\nu}_2 + \tilde{\nu}_3$  matches a two-photon transition from the  $X(v'' = 3, N'')$  state to the  $3d\delta_{5/2}(v = 2, J)$  state, instead of the dips observed when  $\tilde{\nu}_2$  is resonant. The reason for this behavior resides in the fact that one of the states in the double-resonance scheme is a continuum with a bandwidth ( $18(4)\text{ cm}^{-1}$  [17]) that is much larger than the other characteristic frequencies of the system, such as the Rabi frequencies or the laser detunings. To illustrate this conclusion, we use a simple model, depicted in Fig. 4, which follows the lines of Fano's treatment of the effect of the coupling between a discrete state and a continuum on the shape of lines observed in photoexcitation spectra [40].

We consider isolated initial  $X(v'', N'')$ , intermediate  $A_{\Omega'}(v', J')$  and final  $3d\delta_{\Omega}(v, J)$  states, and approximate the  $3d\pi_{\Omega_d}(v_d)$  continuum by a continuum of infinite bandwidth. The lasers are tuned such that  $\tilde{\nu}_2 + \tilde{\nu}_3$  matches the wave number of the  $3d\delta \leftarrow X$  two-photon transition. When laser 2 is off resonance with respect to the  $A \leftarrow X$  transition, the two-photon matrix elements coupling the  $X$  and  $3d\delta$  states and the  $3d\pi$  continuum can be written, within second-order perturbation theory, as

$$\langle f | T^{(2)} | i \rangle = \frac{V_{A-f} V_{A-i}}{E_i - E_A + \omega_k}, \quad (10)$$

where  $i$  stands for the  $X$  or  $3d\delta$  states and  $f$  stands for the  $3d\delta$  or  $3d\pi$  states.  $\omega_k$  is the photon angular frequency of laser 2 ( $k = 2$ ) when  $i$  represents the  $X$  state and that of laser 3 ( $k = 3$ ) when  $i$  represents the  $3d\delta$  state.  $V_{\alpha-\alpha'}$  are the laser field–molecule interaction matrix elements, which are given by Eq. (4) for transitions involving bound states. For transitions to continuum states, the final-state vibrational wave function  $\chi_{v'}^{\alpha'}$  in Eq. (4) must be replaced by an energy-normalized continuum wavefunction (see, e.g., Ref. [50]).

In the experiment, the pulse energies of lasers 3 and 4 are more than one order of magnitude larger than the pulse energy of laser 2, such that the coupling between the  $3d\delta$  state and the  $3d\pi$  continuum is by far the strongest. The problem is thus reduced to the treatment of the excitation from an initial

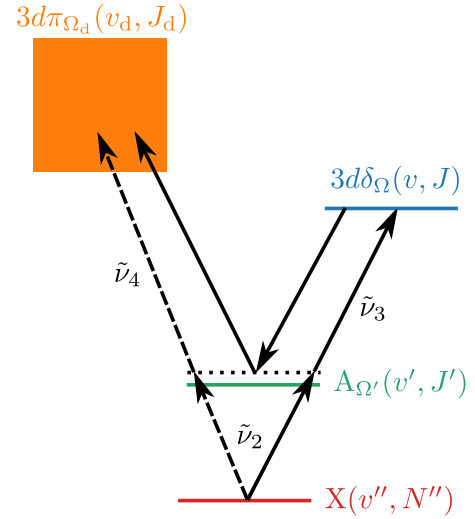


FIG. 4. Simplified photoexcitation and photodissociation scheme used to rationalize the strong effect of  $\tilde{\nu}_2$  on the lineshapes of the  $3d\delta_{\Omega}(v \leq 14)$  vibrational levels of  $\text{MgAr}^+$ . Isolated rovibrational levels of the  $X$ ,  $A_{\Omega'}$ , and  $3d\delta_{\Omega}$  states are considered for simplicity, and the  $3d\pi_{\Omega_d}$  predissociative state is described as a flat continuum of infinite bandwidth. The arrows show the two major interfering photoexcitation pathways to the  $3d\pi_{\Omega_d}$  continuum, which lead to the observed asymmetric lineshapes (see text). The direct two-photon pathway is denoted by the dashed arrows and the indirect four-photon pathway *via* the  $3d\delta_{\Omega}$  state is shown by the full arrows. The horizontal dotted line represents the virtual state through which two-photon excitation proceeds.

state to a bound state that is strongly coupled to a continuum. In contrast to the situation discussed in Ref. [40], the latter coupling is not mediated by configuration interaction but is induced by laser light.

Following Fano's treatment [40], we expect the lineshape associated with the two-photon  $3d\delta \leftarrow X$  transition to be asymmetric as a result of interferences between the two different quantum paths leading to the same final continuum state: (i) the path corresponding to direct two-photon excitation to the  $3d\pi$  continuum (dashed arrows in Fig. 4) and (ii) the four-photon path to the predissociation continuum *via* the  $3d\delta$  state (full arrows in Fig. 4). The asymmetry is governed by the Fano  $q$  parameter which can be written, for the present model, as [40]

$$q = \frac{\langle 3d\delta | T^{(2)} | X \rangle + \mathcal{P} \int d\epsilon' \frac{\langle 3d\delta | T^{(2)} | 3d\pi, \epsilon' \rangle \langle 3d\pi, \epsilon' | T^{(2)} | X \rangle}{\epsilon - \epsilon'}}{\pi \langle 3d\delta | T^{(2)} | 3d\pi, \epsilon \rangle \langle 3d\pi, \epsilon | T^{(2)} | X \rangle}, \quad (11)$$

where  $\epsilon$  is the kinetic energy of the dissociation fragments and  $\mathcal{P} \int$  represents the Cauchy principal value. We assume that the Rabi frequency of the  $3d\pi \leftarrow A$  transition is independent of the wave number  $\tilde{\nu}_4$  of laser 4, which governs the kinetic energy of the dissociation fragments, such that the Cauchy principal value in Eq. (11) is zero. Replacing the matrix elements by their expressions [see Eq. (10)] and using the fact that lasers 2 and 3 are resonant with the  $3d\delta \leftarrow X$ , two-photon transition yields the following expression for the  $q$  parameter

at resonance,

$$q_{\text{res}} \sim \frac{E_X + \omega_2 - E_A}{V_{3d\pi, \epsilon-A}^2}. \quad (12)$$

$V_{3d\pi, \epsilon-A}^2$  is the square of the matrix element coupling the intermediate  $A$  state to the dissociation continuum and has the dimension of an energy because of the energy normalization of the continuum vibrational wave function.

Equation (12) provides an explanation for the different lineshapes we observed for different  $\tilde{\nu}_2$  values [see Fig. 3(b)]. When the detuning between  $\tilde{\nu}_2$  and the resonance wave number of the  $A_{\Omega'}(v', J') \leftarrow X(v'', N'')$  transition is large, and in particular much larger than  $V_{3d\pi, \epsilon-A}^2$ , the  $q$  parameter is large. The associated lineshape is thus close to Lorentzian. The two-photon resonance with a  $3d\delta_{5/2}(v, J)$  state produces an *increase* of the predissociation signal (cases 1 and 4 in Fig. 3). When the detuning is small, the  $q$  parameter is close to zero and the  $3d\delta_{5/2}(v, J)$  states appear as window resonances, i.e., as dips in the predissociation signal [panel 3 in Fig. 3(b)]. At intermediate detunings, the  $q$  parameter is close to unity and the lineshapes are strongly asymmetric [panel 2 in Fig. 3(b)].

The present model attributes the lineshapes to the result of quantum interferences between the direct two-photon-dissociation pathway and the four-photon pathway via  $3d\delta_{\Omega}(v, J)$  intermediate states. The wave number  $\tilde{\nu}_2$  of laser 2 influences the relative phase shift between the pathways, which leads to constructive or destructive interferences and, overall, control over the lineshape. The model only provides a qualitative description of the phenomenon because of the approximations we made. The effective Hamiltonian approach described in Sec. III must be used in order to carry out a quantitative analysis of the spectra, as described in the following section.

The present photoexcitation and photodissociation scheme is similar to quantum-control schemes developed by other authors [22,23,38,39] and is also related to schemes used to generate laser-induced continuum structures [51,52]. These schemes all rely on the interference between different multiphoton excitation and dissociation or ionization pathways. The use of the laser wave number as control parameter significantly simplifies experimental work, because other parameters such as the laser intensities may vary across the interaction volume and the relative laser phases are difficult to control precisely.

### B. Quantitative analysis of the spectra of the $3d\delta_{\Omega}(v \leq 14)$ levels

The experimental spectra of the  $3d\delta_{5/2}(v = 2) \leftarrow X(v'' = 3)$  two-photon transition already displayed in Fig. 3 are compared in Fig. 5 to the spectra calculated with the effective Hamiltonian approach detailed in Sec. III. The calculated spectra reproduce the main spectral features observed experimentally and their dependence on  $\tilde{\nu}_2$ . The agreement between the measured and calculated lineshapes is good. Small discrepancies in the relative strengths of the predissociation signals are attributed to the imperfect modeling of the experimental conditions, the omission of higher order effects such as nonresonant AC Stark shifts, and shot-to-shot fluctuations of the MgAr density and laser-pulse energies in the experiment. The good overall agreement makes us confident

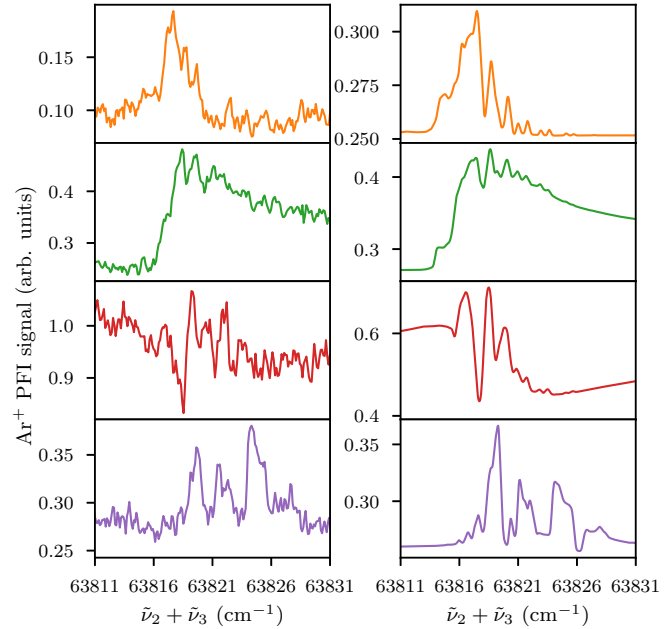


FIG. 5. Experimental (left column) and theoretical (right column) spectra of the  $3d\delta_{5/2}(v = 2) \leftarrow X(v'' = 3)$  two-photon transition for the same wave numbers  $\tilde{\nu}_2$  of laser 2 as in Fig. 3. The labeling and color coding is also identical. The theoretical spectra were scaled by a global factor and offset along the vertical axis to account for the presence of a small background signal in the experimental spectra.

that our model correctly describes the dynamical processes at play.

The effective Hamiltonian approach assumes that the radiation from lasers 2–4 is perfectly coherent. This is not the case in the experiment because the lasers are not monomode ( $\approx 0.1 \text{ cm}^{-1}$  bandwidth,  $\tau_c \approx 0.3 \text{ ns}$  coherence lifetime) and their relative phases are not well defined. In previous studies [22,39], extensive theoretical and experimental work has been carried out to clarify the influence of laser incoherence on the photodissociation of  $\text{Na}_2$  using a quantum-control scheme similar to the one used in the present work. These studies have demonstrated that (i) the relative phases of the different laser beams have no influence on the photodissociation dynamics and (ii) time-varying phases, such as those caused by mode hopping in dye-laser optical cavities, do not significantly influence the dynamics either [22,39], in line with the fact that our coherent model accurately reproduces the experimental results.

The interaction between the ion core and the Rydberg electron can also lead to incoherent effects not taken into account in our model. The Rydberg electron is excited by the first laser to Rydberg states with principal quantum numbers around  $n = 130$ . At such high  $n$  values, Rydberg states with different orbital angular momentum quantum numbers are mixed by the stray electric fields present in the experimental chamber [53]. The timescale associated with the inverse energy density of Stark states beyond the Inglis-Teller limit [54],  $n^4/(2Rc) \approx 43 \text{ ns}$ , is much larger than the duration of the laser pulses used in the experiment ( $\approx 5 \text{ ns}$ ). We therefore do not expect the interaction with the Rydberg electron to significantly affect the spectra we recorded, in agreement with our previous work on

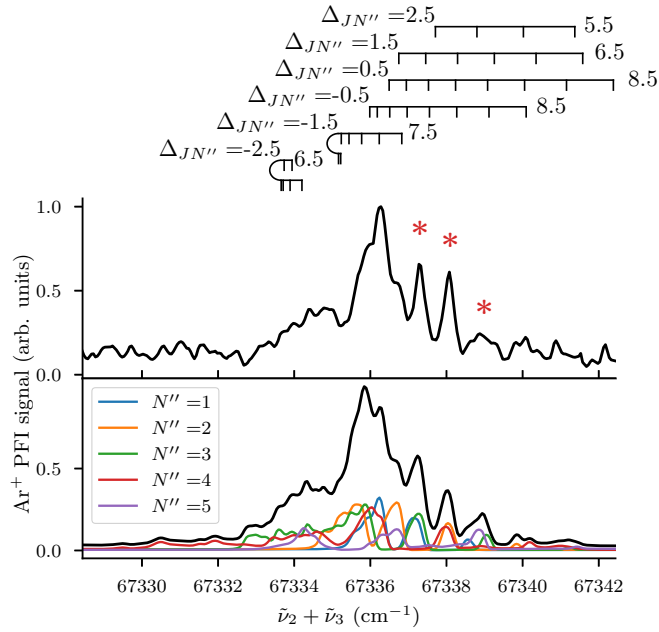


FIG. 6. Measured (top) and calculated (bottom) spectra of the  $3d\delta_{5/2}(v=13) \leftarrow X(v''=3)$  two-photon transition of  $\text{MgAr}^+$ . The contributions of different initial  $N''$  rotational states to the spectrum are also shown in the bottom panel (thin colored lines). They account for about 90% of the total spectrum (thick black line). The assignment bars above the spectra give the positions of the transitions to levels of the  $3d\delta_{5/2}$  state of increasing values of  $J$  for each of the six  $\Delta_{JN''} = J - N''$  branches. The asterisks in the top panel indicate the narrow lines used to extract the band origin  $\tilde{\nu}_{v''}$  and rotational constant  $B_v$  of the upper state.

$\text{Mg}$  [53] and  $\text{MgAr}$  [18], which emphasized the pure spectator role of the Rydberg electron under such conditions.

The rotational structure of the bands shown in Fig. 5 is partially resolved, which makes it possible to extract the value of the band origin and rotational constant of the  $3d\delta_{5/2}(v)$  level under consideration. The easiest approach is to choose  $\tilde{\nu}_2$  values that are detuned from any  $A_{3/2}(v'=5, J') \leftarrow X(v''=3, N'')$  transition [panels 1 and 4 in Fig. 3(b)] because, in such cases, several  $3d\delta_{5/2}(v=2, J)$  states appear as clear lines in the spectra. The signal-to-background ratio is typically greater than 1 and the influence of statistical fluctuations of the background is reduced compared to the other cases (see panels 2 and 3 in Fig. 3).

Figure 6 shows a detailed comparison of experimental and theoretical spectra of the  $3d\delta_{5/2}(v=13) \leftarrow X(v''=3)$  band. The spectra from the different initial rotational states  $N''$  are shown as thin colored lines in the bottom panel. Initial states with  $N'' > 5$  do not contribute significantly to the spectrum. Whereas the low-wave-number side of the band is composed of broad unresolved structures, the high-wave-number side shows sharp lines that can be assigned to only one or a few rotational transitions. These lines are marked by asterisks in the top panel. For example, the line at  $67\,337.3\text{ cm}^{-1}$  is attributed to the overlapping  $J = \frac{5}{2} \leftarrow N'' = 1$  and  $J = \frac{7}{2} \leftarrow N'' = 3$  transitions. A direct fit of the calculated spectrum to the experimental spectrum to determine the band origin and rotational constant is computationally prohibitively expensive.

Instead, the wave numbers of the narrow lines were obtained from a least-squares fit to Beutler-Fano lineshapes. The rotational constant  $B_v$  of the  $3d\delta_{5/2}(v=13)$  state and the band origin  $\tilde{\nu}_{v''}$  of the transition were then determined in another least-squares fit based on the standard expression

$$\tilde{\nu} = \tilde{\nu}_{v''} + B_v[J(J+1) - \Omega^2] - B''_v N''(N''+1). \quad (13)$$

The rotational constant  $B''_3$  of the  $X(v''=3)$  state was fixed to its experimental value ( $0.12727(9)\text{ cm}^{-1}$  [16]).

The values obtained from the fit are listed in Table I, together with the values for all the other bands we measured. Because the lines are blended, inherently asymmetric, and the spectrum is congested, the line positions are potentially affected by systematic errors. In order to assess the importance of such errors, we fitted the theoretical spectrum using the same procedure as used for the experimental spectrum and compared the values we obtained with the transition wave numbers used in the calculation. Typical differences of  $\approx 0.1\text{ cm}^{-1}$  or less resulted, which is small compared to other sources of uncertainties. We also determined  $\tilde{\nu}_{v''}$  and  $B_v$  for several spectra of the same vibrational band recorded at different  $\tilde{\nu}_2$  values, as shown in Fig. 3. The standard deviations of the results,  $\sigma_{\tilde{\nu}_{v''}} = 0.35\text{ cm}^{-1}$  and  $\sigma_{B_v} = 0.009\text{ cm}^{-1}$ , respectively, were taken as the statistical uncertainties when vibrational bands were measured only for a single value of  $\tilde{\nu}_2$ . Otherwise, the standard deviation of the mean is reported as statistical uncertainty.

### C. Experimental spectra and analysis of the $3d\delta_{3/2}(v \geq 15)$ levels

Above  $v=15$ , the vibrational levels of the  $3d\delta_{3/2}$  states predissociate directly into the  $\text{Mg}(3s^2) + \text{Ar}^+(3p^5)$  charge-transfer continua (see Fig. 1). Consequently, in this range, the spectra can be recorded by ICMRD without laser 4. No predissociation signal could be observed for the  $3d\delta_{5/2}$  vibrational levels. The charge-transfer states have  $\Omega$  values of  $1/2$  and  $3/2$  and this observation demonstrates that heterogeneous couplings ( $\Delta\Omega = \pm 1$ ) are weak in the range of total angular momenta probed experimentally ( $J \lesssim 10$ ). Homogeneous perturbations ( $\Delta\Omega = 0$ ), on the other hand, are typically larger and responsible for the predissociation of the  $3d\delta_{3/2}(v \geq 15)$  levels.

The position of the  $3d\delta_{3/2}(v=15)$  level is marked by the dashed horizontal line in Fig. 1 and lies in the energy range where the potential-energy curve of the  $3d\delta_{3/2}$  state is crossed by the repulsive part of the potential of the charge-transfer state with  $\Omega_d = 3/2$ . The predissociation widths of the  $3d\delta_{3/2}(v)$  states are small ( $\lesssim 0.2\text{ cm}^{-1}$ ) such that the rotational structures of the  $3d\delta_{\Omega}(v) \leftarrow A_{\Omega'}(v', J')$  bands are partially resolved. The spectrum of the  $3d\delta_{\Omega}(v=15, J) \leftarrow A_{\Omega'}(v'=10, J' = \frac{1}{2}, \frac{3}{2}, \frac{5}{2}, \frac{7}{2})$  transitions is shown as illustration in Fig. 7. The initial states were prepared by excitation from the  $X(v''=3)$  state with laser 2 tuned to  $\tilde{\nu}_2 = 33\,521.60\text{ cm}^{-1}$ . The spectrum was analyzed as explained in Ref. [17] to obtain the band origin and rotational constant of the  $3d\delta_{\Omega}(v=15)$  state listed in Table I. No ICMRD spectra could be recorded for the  $v=27, 30$ , and  $34$  vibrational levels, most likely because their predissociation is slower than

TABLE I. Band origins of the  $3d\delta_{\Omega}(v) \leftarrow X(v'')$  two-photon transitions ( $\tilde{\nu}_{vv''}$ ,  $v \leq 14$ ) and of the  $3d\delta_{\Omega}(v) \leftarrow A_{1/2}(v')$  one-photon transitions ( $\tilde{\nu}_{vv'}$ ,  $v > 14$ ), term values  $T_v^{\Omega}$  of the  $3d\delta_{\Omega}(v)$  vibrational levels relative to the  $3d\delta_{5/2}(v=0)$  ground state, and corresponding rotational constants  $B_v^{\Omega}$  of  $^{24}\text{Mg}^{40}\text{Ar}^+$ .  $\Delta T_v^{\Omega} = T_v^{\Omega}(\text{exp}) - T_v^{\Omega}(\text{calc})$  and  $\Delta B_v^{\Omega} = B_v^{\Omega}(\text{exp}) - B_v^{\Omega}(\text{calc})$  give the differences between the term values and rotational constants extracted from experimental data and those calculated using the potential-energy functions determined in this article. All values are in  $\text{cm}^{-1}$  and the numbers in parentheses represent one standard deviation in units of the last digit. The absolute term values above the  $X(v''=0)$  ground state can be obtained by adding  $T_{X(0)-3d\delta_{5/2}(0)} = 63\,430.16(150) \text{ cm}^{-1}$  to  $T_v^{\Omega}$ .  $T_{X(0)-3d\delta_{5/2}(0)}$  was obtained using the term value of the  $X(v''=3)$  state reported in Ref. [41].

$v$	$v'$	$v''$	$\Omega$	$\tilde{\nu}_{vv''}/\tilde{\nu}_{vv'}$	$T_v^{\Omega}$	$\Delta T_v^{\Omega}$	$B_v^{\Omega}$	$\Delta B_v^{\Omega}$
0		3	5/2	63145.36(35)	0.0(5)	0.44	0.228(15)	0.026
0		3	3/2	63151.41(35)	6.1(5)	0.26	0.254(9)	-0.001
2		3	5/2	63817.96(35)	672.6(5)	0.12	0.210(9)	-0.007
2		3	3/2	63823.42(35)	678.1(5)	0.41	0.216(9)	-0.014
4		3	5/2	64464.92(35)	1319.6(5)	-0.35	0.208(9)	-0.006
4		3	3/2	64470.55(35)	1325.2(5)	-0.36	0.212(9)	-0.011
6		3	5/2	65088.01(35)	1942.7(5)	-0.54	0.201(9)	0.014
6		3	3/2	65093.20(35)	1947.8(5)	-0.25	0.227(11)	-0.012
8		3	5/2	65686.26(35)	2540.9(5)	-0.36	0.196(9)	-0.002
8		3	3/2	65691.43(35)	2546.1(5)	-0.19	0.206(9)	-0.012
10		3	5/2	66259.61(35)	3114.2(5)	-0.35	0.199(9)	-0.003
10		3	3/2	66264.62(35)	3119.3(5)	-0.18	0.200(9)	-0.004
12		3	5/2	66808.23(35)	3662.9(5)	-0.08	0.186(9)	-0.002
12		3	3/2	66813.09(35)	3667.7(5)	0.06	0.196(9)	-0.012
13		3	5/2	67073.00(35)	3927.6(5)	-0.22	0.200(9)	0.003
13		3	3/2	67077.66(37)	3932.3(5)	0.05	0.198(13)	0.005
14		3	5/2	67331.49(35)	4186.1(5)	0.04	0.191(9)	-0.001
14	10	3	3/2	33814.60(4)	4190.8(4)	-0.10	0.1922(9)	0.0001
15	10	3	3/2	34066.79(4)	4443.0(4)	-0.01	0.1893(9)	-0.0000
16	10	3	3/2	34312.61(4)	4688.8(4)	0.05	0.1867(9)	0.0001
17	10	3	3/2	34552.04(4)	4928.3(4)	0.09	0.184(2)	0.000
18	10	3	3/2	34785.08(4)	5161.3(4)	0.14	0.178(3)	-0.003
19	14	7	3/2	34250.90(4)	5387.9(4)	0.20	0.1761(13)	-0.0019
20	14	7	3/2	34470.99(6)	5608.0(4)	0.17	0.173(3)	-0.002
21	14	7	3/2	34684.62(4)	5821.7(4)	0.16	0.173(2)	0.001
22	14	7	3/2	34891.67(4)	6028.7(4)	0.10	0.1699(14)	0.0009
23	19	7	3/2	34297.25(4)	6229.0(4)	-0.12	0.1684(14)	0.0025
24	19	3	3/2	34491.31(4)	6423.1(4)	-0.00	0.1612(9)	-0.0016
25	19	3	3/2	34678.50(4)	6610.3(4)	-0.12	0.1591(9)	-0.0005
26	19	3	3/2	34849.09(8)	6780.9(4)	-10.16	0.1559(9)	-0.0005
28	26	7	3/2	34385.66(12)	7131.9(4)	-0.16	0.150(4)	0.001
29	26	7	3/2	34545.98(11)	7292.3(4)	-0.21	0.148(3)	0.002
31	26	7	3/2	34846.31(8)	7592.6(4)	-0.09	0.140(2)	0.001
32	26	7	3/2	34986.16(9)	7732.4(4)	-0.04	0.140(3)	0.005
33	26	7	3/2	35119.40(10)	7865.7(4)	0.28	0.135(3)	0.003
35	26	7	3/2	35362.42(4)	8108.7(4)	-1.86	0.1285(9)	0.0046
36	26	7	3/2	35476.41(19)	8222.7(5)	-0.15		

other decay mechanisms, such as, for example, fluorescence to lower lying electronic states.

#### D. Characterization of the $3d\delta$ state of $\text{MgAr}^+$

Molecular constants characterizing all vibrational levels of the  $3d\delta_{\Omega}$  states of  $\text{MgAr}^+$  studied experimentally are listed in Table II. Both spin-orbit components of the  $3d\delta$  state asymptotically correlate to the  $\text{Mg}^+(3d_{5/2}) + \text{Ar}(^1S_0)$  dissociation limit. The dissociation energies  $D_0(3d\delta_{\Omega})$  were calculated using the thermodynamic cycle

$$\frac{D_0(3d\delta_{\Omega})}{hc} = \tilde{\nu}_{\text{Mg}^+(3p_{1/2}-3d_{5/2})} + \frac{D_0(A_{1/2})}{hc} - \tilde{\nu}_{v=0, v''=3}^{\Omega} + \tilde{\nu}_{v'=0, v''=3}, \quad (14)$$

where  $\tilde{\nu}_{\text{Mg}^+(3p_{1/2}-3d_{5/2})}$  is the wave number of the  $3p_{1/2} - 3d_{5/2}$  dipole-forbidden transition in atomic  $\text{Mg}^+$ , taken from the NIST database [55],  $D_0(A_{1/2})$  is the dissociation energy of the  $A_{1/2}$  state [16],  $\tilde{\nu}_{v=0, v''=3}^{\Omega}$  are the wave numbers of the  $3d\delta_{\Omega}(v=0) \leftarrow X(v''=3)$  two-photon transitions ( $\Omega = 3/2, 5/2$ ) measured in this work (see Table I), and  $\tilde{\nu}_{v'=0, v''=3}$  is the wave number of the  $A_{1/2}(v'=0) \leftarrow X(v''=3)$  band origin [16].

Theoretical values for  $D_0$  are limited to those calculated from the *ab initio* potential-energy functions reported in Ref. [15] (9235.5 and 9241.4  $\text{cm}^{-1}$  for  $\Omega = \frac{3}{2}$  and  $\frac{5}{2}$ , respectively). They are in good agreement with the experimental ones. The harmonic ( $\omega_e$ ) and anharmonic ( $\omega_e x_e$ ,  $\omega_e y_e$ , and  $\omega_e z_e$ ) vibrational constants as well as the equilibrium

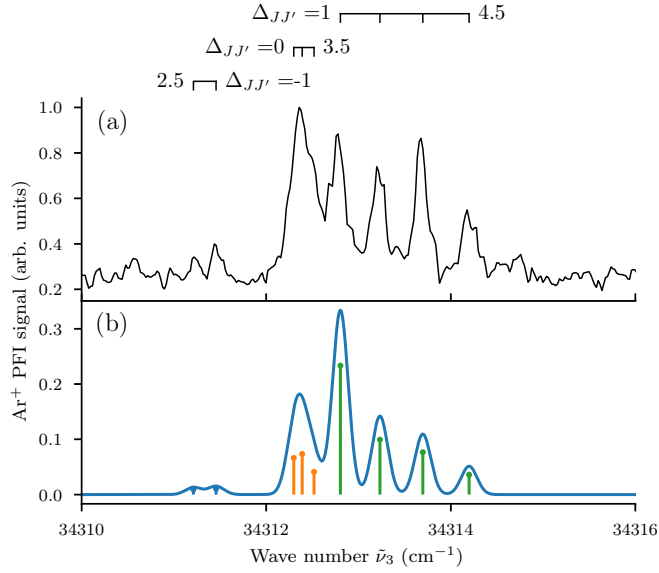


FIG. 7. Experimental (a) and calculated (b) spectra of the  $3d\delta_{3/2}(v=15) \leftarrow A_{1/2}(v'=10)$  transition recorded by ICMRD. The rotational states of the  $A_{1/2}(v'=10)$  level with  $J' = \frac{1}{2}, \frac{3}{2}, \frac{5}{2}$ , and  $\frac{7}{2}$  were prepared by photoexcitation from the  $X(v''=3)$  ground electronic state and their relative populations were estimated to be 1, 0.7, 0.7, and 0.4, respectively. The assignment bars shown above the spectra and the stick spectrum in the lower panel give the positions of the transitions to levels of the  $3d\delta_{3/2}$  state of successive values of  $J$ . See Ref. [17] for details on the calculation of the spectrum.

rotational constant  $B_e$  and the rotation-vibration coupling constant  $\alpha_e$  were obtained in least-squares fits of the term values  $T_v$  and rotational constants  $B_v$  to the usual polynomial expansions [43]

$$T_v = T_e + \omega_e \left( v + \frac{1}{2} \right) - \omega_e x_e \left( v + \frac{1}{2} \right)^2 + \omega_e y_e \left( v + \frac{1}{2} \right)^3 + \omega_e z_e \left( v + \frac{1}{2} \right)^4 \quad (15)$$

TABLE II. Molecular constants of the  $3d\delta_\Omega$  states of  $^{24}\text{MgAr}^+$  derived from experimental data and parameters describing the potential-energy functions of the  $3d\delta_{3/2}$  and  $3d\delta_{5/2}$  states according to Eqs. (17)–(20). All molecular constants are in  $\text{cm}^{-1}$  and the numbers in parentheses represent one standard deviation in units of the last digit. The parameters of the potential-energy functions are given in atomic units.

	$3d\delta_{3/2}$		$3d\delta_{5/2}$		Potential parameters			
	Experiment	Theory [15]	Experiment	Theory [15]	$V_\Delta(R)$		$a(R)$	
$D_0$	9299.9(11)	9235.5	9305.9(11)	9241.4	$R_e$	$4.18104 a_0$	$E$	$-9.64 \times 10^{-8} E_h$
$T_e$	62979.9(5)		62973.4(6)		$D_e$	$0.043172 E_h$	$F$	$1.2 a_0^{-1}$
$\omega_e$	344.92(11)	344.03	345.47(15)	344.47	$B$	$1.22424 a_0^{-1}$	$G$	$6.3 a_0$
$\omega_e x_e$	3.033(12)	3.043	3.096(9)	3.099	$\rho$	$0.47282 a_0^{-1}$	$D$	0.28577
$\omega_e y_e$	-0.0018(4)							
$\omega_e z_e$	0.000042(6)							
$B_e$	0.2364(10)	0.2235	0.216(7)	0.220				
$\alpha_e$	0.00303(4)	0.00283	0.0018(7)	0.0025				

and

$$B_v = B_e - \alpha_e \left( v + \frac{1}{2} \right). \quad (16)$$

The  $3d\delta_\Omega$  states are almost as strongly bound as the ground electronic state of the  $\text{MgAr}^{2+}$  dication ( $D_0^{X^{2+}} = 10\,690(3) \text{ cm}^{-1}$  [10]). Both states also have similar molecular constants ( $\omega_e^{X^{2+}} = 327.02(11) \text{ cm}^{-1}$ ,  $\omega_e x_e^{X^{2+}} = 2.477(15) \text{ cm}^{-1}$  [10], and  $B_e^{X^{2+}} = 0.209 \text{ cm}^{-1}$  [56]). This similarity highlights the Rydberg character of the  $3d\delta_\Omega$  states. Indeed, Rydberg states have potential-energy functions that closely match the potential-energy functions of the ionized species to which the Rydberg series converge. The effective principal quantum number associated with the lowest vibrational levels of the  $3d\delta_\Omega$  states is  $n^* \simeq 3.01$ . This translates into a mean radial distance of the  $3d$  Rydberg electron of  $\bar{r} \simeq 5.3 a_0$  ( $2.8 \text{ \AA}$ ) [54], which is larger than the equilibrium bond length of the doubly charged ion core ( $R_e \simeq 4.380 a_0$  [56]).

The  $3d\pi_\Omega$  states, which also belong to the  $3d$  Rydberg complex of  $\text{MgAr}^+$ , are less strongly bound ( $5944.7(10)$  and  $5907.7(10) \text{ cm}^{-1}$  for  $\Omega = 1/2$  and  $3/2$ , respectively [17]). As in the case of the lower lying  $3p$  Rydberg complex, this property can be qualitatively understood by considering the orientation of the  $3d$  orbital of  $\text{Mg}^+$  with respect to the internuclear axis [16,47]. Whereas the  $3d\delta$  orbital ( $m_l = 2$ ) leaves the neutral Ar atom exposed to the doubly charged  $\text{Mg}^{2+}$  core, the  $3d\pi$  ( $m_l = 1$ ) orbital, and to a greater extent the  $3d\sigma$  ( $m_l = 0$ ) orbital, partially shield the doubly charged core. Electrostatic interactions, which make a dominant contribution to the total binding of the molecular ion, are thus more pronounced in the case of the  $3d\delta$  states and their dissociation energies are significantly larger.

When the Rydberg-electron radial distance is comparable to the bond length of the molecule, as is the case for the  $3d$  Rydberg complex of  $\text{MgAr}^+$ , the potential-energy functions of the corresponding molecular electronic states are significantly affected by the scattering of the Rydberg electron onto the neutral atom [57–59]. Studies of the low-lying Rydberg states of the rare-gas dimers showed that the repulsive exchange interaction between the Rydberg electron and the neutral atom is responsible for the presence of local maxima in the potential-energy function, at internuclear distances

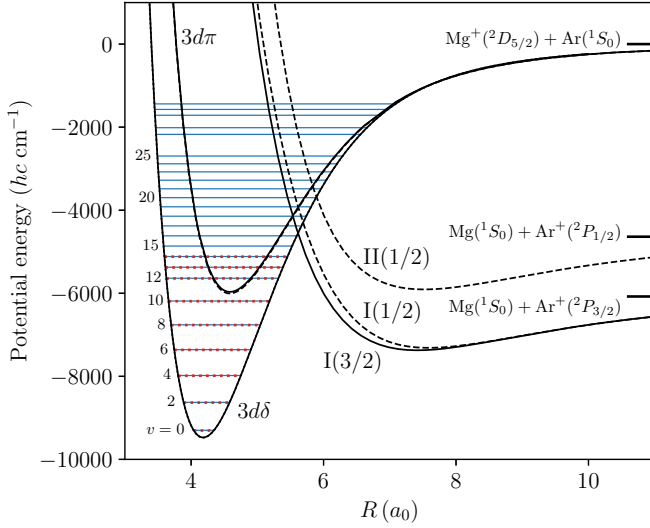


FIG. 8. Potential-energy functions of the  $3d\pi_{1/2,3/2}$  states [15], the  $3d\delta_{3/2,5/2}$  states (present work), and the  $\text{Mg}^+(^1S_0) + \text{Ar}^+(^2P_{1/2,3/2})$  charge-transfer states [17] of  $\text{MgAr}^+$ . The  $3d\delta_{3/2}$  and  $3d\delta_{5/2}$  states are indistinguishable on the scale of the figure. At internuclear distances below their equilibrium distances, charge-transfer states with  $\Omega_d = 1/2$  and  $\Lambda_d = 0$  and 1 are strongly mixed by the spin-orbit interaction. The charge-transfer curves are thus labeled by an index (I or II) specifying their dissociation limit and by  $\Omega_d$ . The vibrational levels of the  $3d\delta_{3/2}$  and  $3d\delta_{5/2}$  states measured in the present work are shown by the blue full horizontal lines and red dotted horizontal lines, respectively. Vibrational states of the  $3d\delta_{3/2}$  state with  $v \geq 15$  predissociate into the charge-transfer continua.

close to the maxima of the Rydberg-electron probability density [59,60]. Because of its orientation in the molecule-fixed frame, the amplitude of the  $3d\delta$  orbital, which is centered onto the  $\text{Mg}^+$  ion, is negligible at the position of the Ar atom and the effect discussed above does not play a significant role. Indeed, the potential-energy functions of the  $3d\delta$  state are, as discussed above, very close to the one of the doubly charged ion core and do not exhibit any local maxima (see Figs. 1 and 8). In contrast, a Rydberg electron in a  $3d\sigma$  orbital has a non-negligible probability to be located at the position of the Ar atom. The potential-energy function of the corresponding molecular electronic state significantly differs from the one of  $\text{MgAr}^{2+}$  (see Fig. 1) and displays a local maximum. Further investigation is required to assess whether this maximum is solely caused by the scattering of the  $3d\sigma$  Rydberg electron onto the Ar atom.

### E. Potential-energy functions

Accurate potential-energy functions describing the  $3d\delta_{3/2}$  and  $3d\delta_{5/2}$  electronic states were determined from the measured energies and rotational constants using a direct potential fit approach [61], following a procedure similar to the one we used for the  $3p$  Rydberg complex of  $\text{MgAr}^+$  [16]. Whereas strong nonadiabatic effects made this approach impractical for the  $3d\pi_{\Omega_d}$  states of  $\text{MgAr}^+$  [17], the regular progressions of vibrational levels we recorded in the present work makes it possible to determine potential-energy functions from a nonlinear least-squares fit to the experimental data.

The potential-energy functions of the two spin-orbit components of the  $3d\delta$  state are expressed as

$$V_{3/2}(R) = V_{\Delta}(R) - a(R) \text{ and } V_{5/2}(R) = V_{\Delta}(R) + a(R), \quad (17)$$

where  $V_{\Delta}(R)$  is the potential-energy function of the  $3d\delta$  state without spin-orbit interaction and  $a(R)$  is the  $R$ -dependent spin-orbit coupling constant. Deviations from Eq. (17) are expected at large internuclear distances  $R$ , where the magnitudes of the spin-orbit and electrostatic interactions become comparable and the spin-orbit interaction couples states of different projections ( $\hbar\Lambda$ ) of the electronic orbital angular momentum but identical projections  $\hbar\Omega$  of the total angular momentum (i.e., the  $3d\pi_{3/2}$  and  $3d\delta_{3/2}$  states in the present case). However, the spin-orbit coupling constant in the  $3d$  Rydberg complex is very small, as demonstrated by the small spin-orbit splittings we measured ( $< 6 \text{ cm}^{-1}$ , see Table I), such that only the vibrational levels lying very close to the dissociation threshold ( $\lesssim 10 \text{ cm}^{-1}$ ) are affected.

The  $\Delta$ -state potential-energy function  $V_{\Delta}(R)$  is represented by a function of the form

$$V_{\Delta}(R) = A \exp \left[ -2 \left( B + D \frac{R^5 - R_{\text{ref}}^5}{R^5 + R_{\text{ref}}^5} \right) (R - R_e) \right] - C \exp \left[ - \left( B + D \frac{R^5 - R_{\text{ref}}^5}{R^5 + R_{\text{ref}}^5} \right) (R - R_e) \right] + u_{\text{LR}}(R; \rho), \quad (18)$$

analogous to the double-exponential/long-range (LR) model potential described by Le Roy [61].  $A$ ,  $B$ ,  $C$ , and  $D$  are adjustable parameters. Their relationship to the equilibrium distance  $R_e$  and potential-well depth  $D_e$  is given in Ref. [16]. In the present study, we fixed  $R_{\text{ref}} = 7.2 a_0$ , a value at which the least-squares fit converged rapidly and with the smallest number of adjustable parameters. In Eq. (18), the long-range behavior of the potential is described by the function  $u_{\text{LR}}(R)$ , which includes the dominant electrostatic interactions between  $\text{Mg}^+(3d, m_l = \Lambda)$  and Ar,

$$u_{\text{LR}}(R; \rho) = -\frac{\alpha_{\text{Ar}}}{2R^4} \phi^{(4)}(R; \rho) - \frac{C_6}{R^6} \phi^{(6)}(R; \rho). \quad (19)$$

The damping functions  $\phi^{(m)}(R; \rho)$  progressively switch off long-range electrostatic interactions at short internuclear distances. They depend parametrically on the system-dependent range-scaling parameter  $\rho$ , which is an adjustable parameter of the model [16,62]. The static electric polarizability volume of the Ar atom ( $\alpha_{\text{Ar}} = 11.077 a_0^3$ ) is taken from Ref. [63]. The  $C_6$  coefficient ( $525.608 E_h a_0^6$ ) is calculated as described in Ref. [16] from the quadrupole polarizability of Ar ( $\alpha_{\text{Ar}}^{(2)} = 50.21 a_0^5$  [64]), the dispersion coefficient ( $C_6^{\text{disp}} = 220.1 E_h a_0^6$  [65]) for the interaction between  $\text{Mg}^+(3d, m_l = 2)$  and Ar, and the quadrupole moment of  $\text{Mg}^+(3d, m_l = 2)$  ( $\Theta_{zz} = 1.819 e a_0^2$  [65]).

The  $R$ -dependent spin-orbit coupling constant is described by the function [16,66]

$$a(R) = E[1 - e^{-F(R-G)}]^2 - E. \quad (20)$$

The parameters  $E$ ,  $F$ , and  $G$  in Eq. (20) are adjustable.  $a(R)$  vanishes at large internuclear distances, in accordance with

the fact that the  $3d\delta_{3/2}$  and  $3d\delta_{5/2}$  converge to the same  $\text{Mg}^+(3d_{5/2}) + \text{Ar}$  dissociation threshold.

Term values and rotational constants associated with the potential-energy functions (17) are calculated by solving the nuclear Schrödinger equation as described in Ref. [16]. Optimal values of the eight parameters of the model potentials are determined in a weighted nonlinear least-squares fit of the calculated data to the experimental data, which comprise 68 data points in total. The term values of the  $3d\delta_{3/2}(v = 26, 35, 36)$  levels appear perturbed with respect to the regular vibrational progression and were excluded from the fit. The optimal parameter values are listed in Table II, and the calculated vibrational term values and rotational constants are compared to experimental values in Table I. The weighted root-mean-square deviation of the fit is 0.96, indicating that the model potentials adequately describe the experimental data. The potential-energy functions are depicted in Fig. 8 together with those of the  $3d\pi_{1/2,3/2}$  states and the charge-transfer states [17].

## V. CONCLUSION

In this article, we have presented a detailed study of the  $3d\delta_{3/2}$  and  $3d\delta_{5/2}$  Rydberg states of  $\text{MgAr}^+$ . Spectra of the vibrational levels with  $v \leq 14$  were recorded using a multiphoton-dissociation scheme involving the ground electronic state ( $X$ ), the first electronically excited state ( $A_{\Omega'}$ ), the  $3d_{\Omega}$  states, and predissociative vibrational levels of the  $3d\pi_{1/2}$  and  $3d\pi_{3/2}$  states. Using this scheme, lines associated with two-photon  $3d\delta_{\Omega} \leftarrow X$  transitions appeared as predissociation signals and could be recorded with partial rotational resolution, despite the fact that the  $3d\delta_{\Omega}(v \leq 14)$  vibrational levels do not predissociate. Control over the lineshapes was achieved by changing the wave number of the laser driving the  $A_{\Omega'} \leftarrow X$  transition, and exploited the interference between a direct two-photon-excitation pathway and an indirect four-photon pathway to the predissociative state (see Fig. 4). An effective Hamiltonian approach was used to theoretically calculate the predissociation spectra, and the complex lineshapes observed experimentally could be quantitatively reproduced. Experimental spectra were assigned based on the theoretical results, and band origins and rotational constants could be extracted for many vibrational levels of the  $3d\delta$  state of  $\text{MgAr}^+$ . This method is expected to be generally applicable to the study of electronically excited states of molecular ions that do not predissociate.

Spectra of the  $3d\delta_{3/2}(v \geq 15)$  vibrational levels were recorded by ICMRD, exploiting the fact that these levels predissociate into the charge-transfer continua  $\text{Mg}(3s^2) +$

$\text{Ar}^+(3p^5)$ . The absence of predissociation signal for the  $v \geq 15$  vibrational levels of the  $3d\delta_{5/2}$  spin-orbit component prevented their investigation by ICMRD. We attribute the nonpredissociative nature of these levels to the fact that they are only coupled with the charge-transfer continua through heterogeneous  $\Delta\Omega = 1$  interactions. The potential-energy functions of the  $3d\delta_{3/2}$  and  $3d\delta_{5/2}$  states were determined from the experimental data in a direct nonlinear least-squares fit (see Fig. 8).

Charge-transfer interactions, which dominate the dynamics of the  $3d\pi_{1/2,3/2}$  Rydberg states and of the high vibrational levels of the  $4s\sigma_{1/2}$  Rydberg state [17], are much less pronounced in the case of the  $3d\delta_{3/2,5/2}$  states. Whereas predissociation widths as large as  $160(40) \text{ cm}^{-1}$  were observed for the  $3d\pi_{3/2}$  state, corresponding to lifetimes as short as  $33(8) \text{ fs}$ , they are typically below  $\approx 0.1 \text{ cm}^{-1}$  for the  $3d\delta_{3/2}$  state (lifetimes  $\gtrsim 300 \text{ ps}$ ) and negligible in the case of the  $3d\delta_{5/2}$  state. These considerations, combined with the fact that  $\text{Ar}^+ + \text{Mg}$  charge-transfer states possess either a  ${}^2\Pi_{3/2}$  or a mixed  ${}^2\Sigma_{1/2}^+ - {}^2\Pi_{1/2}$  character [17], lead to the following classification for the range of total angular momenta probed experimentally ( $J \lesssim 10$ ): Homogeneous interactions with  $\Delta\Lambda = 0$ , which affect the  $3d\pi$  and  $4s\sigma$  Rydberg states, are the largest; interactions with  $\Delta\Lambda = 1$  but  $\Delta\Omega = 0$ , which affect the  $3d\delta_{3/2}$  state, are weaker; and heterogeneous interactions with  $\Delta\Lambda = \Delta\Omega = 1$  are negligible. Nonadiabatic charge-transfer interactions do not only affect the members of the  $4s$  and  $3d$  complexes but also of all the  $(n+1)s$  and  $nd$  complexes with higher principal quantum numbers ( $n > 3$ ), as explained in Ref. [17]. The present work thus shows that, because the charge-transfer states responsible for the dynamics typically involve low angular momenta ( $\Lambda$  and  $\Omega$  small), Rydberg states associated with a low angular-momentum quantum number  $l$  of the Rydberg electron are likely to be affected by charge-transfer dynamics, whereas the vast majority of the states associated with high- $l$  Rydberg electrons should not be affected. We expect that the conclusions drawn here for  $\text{MgAr}^+$  are generally applicable to the Rydberg states of diatomic cations with thermodynamically stable doubly charged ion cores [17].

## ACKNOWLEDGMENTS

We thank Hansjürg Schmutz and Josef A. Agner for their technical assistance. This work is supported financially by the Swiss National Science Foundation (Grant No. 200020B-200478) and the European Research Council through an ERC advanced grant (Grant No. 743121) under the European Union's Horizon 2020 research and innovation programme.

- 
- [1] R. S. Mulliken, *J. Am. Chem. Soc.* **86**, 3183 (1964).  
 [2] R. S. Mulliken, *J. Am. Chem. Soc.* **88**, 1849 (1966).  
 [3] R. S. Mulliken, *J. Am. Chem. Soc.* **91**, 4615 (1969).  
 [4] G. Herzberg, *Annu. Rev. Phys. Chem.* **38**, 27 (1987).  
 [5] F. Merkt, *Annu. Rev. Phys. Chem.* **48**, 675 (1997).  
 [6] T. P. Softley, *Int. Rev. Phys. Chem.* **23**, 1 (2004).  
 [7] K. Müller-Dethlefs and E. W. Schlag, *Angew. Chem. Int. Ed.* **37**, 1346 (1998).  
 [8] P. M. Johnson and L. Zhu, *Int. J. Mass Spectrom. Ion Process.* **131**, 193 (1994).  
 [9] M. Génévriez, D. Wehrli, J. Agner, and F. Merkt, *Int. J. Mass Spectrom.* **435**, 209 (2019).  
 [10] D. Wehrli, M. Génévriez, and F. Merkt, *Phys. Chem. Chem. Phys.* **23**, 10978 (2021).  
 [11] J. Loreau, S. Ryabchenko, J. M. M. Burgos, and N. Vaeck, *J. Phys. B: At. Mol. Opt. Phys.* **51**, 085205 (2018).

- [12] A. V. Kosarim, B. M. Smirnov, A. Laricchiuta, and M. Capitelli, *Phys. Plasmas* **19**, 062309 (2012).
- [13] J. M. Muñoz Burgos, M. Griener, J. Loreau, A. Gorbunov, T. Lunt, O. Schmitz, and E. Wolfrum, *Phys. Plasmas* **26**, 063301 (2019).
- [14] K. B. MacAdam, J. C. Day, J. C. Aguilar, D. M. Homan, A. D. MacKellar, and M. J. Cavagnero, *Phys. Rev. Lett.* **75**, 1723 (1995).
- [15] D. Wehrli, M. Génévriez, S. Knecht, M. Reiher, and F. Merkt, *J. Chem. Phys.* **153**, 074310 (2020).
- [16] M. Génévriez, D. Wehrli, and F. Merkt, *J. Chem. Phys.* **153**, 074311 (2020).
- [17] D. Wehrli, M. Génévriez, S. Knecht, M. Reiher, and F. Merkt, *J. Phys. Chem. A* (2021), doi: [10.1021/acs.jpca.1c03859](https://doi.org/10.1021/acs.jpca.1c03859).
- [18] M. Génévriez, D. Wehrli, and F. Merkt, *Mol. Phys.* **118**, e1703051 (2020).
- [19] P. O. Danis, T. Wyttenbach, and J. P. Maier, *J. Chem. Phys.* **88**, 3451 (1988).
- [20] Y. Wang, L. Li, and W. A. Chupka, *Chem. Phys. Lett.* **185**, 478 (1991).
- [21] D. J. Tannor, R. Kosloff, and S. A. Rice, *J. Chem. Phys.* **85**, 5805 (1986).
- [22] A. Shnitman, I. Sofer, I. Golub, A. Yogev, M. Shapiro, Z. Chen, and P. Brumer, *Phys. Rev. Lett.* **76**, 2886 (1996).
- [23] Z. Chen, M. Shapiro, and P. Brumer, *Chem. Phys. Lett.* **228**, 289 (1994).
- [24] B. Sheehy, B. Walker, and L. F. DiMauro, *Phys. Rev. Lett.* **74**, 4799 (1995).
- [25] V. D. Kleiman, L. Zhu, J. Allen, and R. J. Gordon, *J. Chem. Phys.* **103**, 10800 (1995).
- [26] B. H. Hosseini, H. R. Sadeghpour, and N. Balakrishnan, *Phys. Rev. A* **71**, 023402 (2005).
- [27] R. J. Gordon and S. A. Rice, *Annu. Rev. Phys. Chem.* **48**, 601 (1997).
- [28] M. Shapiro and P. Brumer, *Rep. Prog. Phys.* **66**, 859 (2003).
- [29] C. Brif, R. Chakrabarti, and H. Rabitz, *New J. Phys.* **12**, 075008 (2010).
- [30] C. P. Koch and M. Shapiro, *Chem. Rev.* **112**, 4928 (2012).
- [31] U. Gaubatz, P. Rudecki, S. Schiemann, and K. Bergmann, *J. Chem. Phys.* **92**, 5363 (1990).
- [32] K. Bergmann, H.-C. Nägerl, C. Panda, G. Gabrielse, E. Miloglyadov, M. Quack, G. Seyfang, G. Wichmann, S. Ospelkaus, A. Kuhn, S. Longhi, A. Szameit, P. Pirro, B. Hillebrands, X.-F. Zhu, J. Zhu, M. Drewsen, W. K. Hensinger, S. Weidt, T. Halfmann *et al.*, *J. Phys. B: At. Mol. Opt. Phys.* **52**, 202001 (2019).
- [33] K. Ohmori, *Annu. Rev. Phys. Chem.* **60**, 487 (2009).
- [34] S. Shi, A. Woody, and H. Rabitz, *J. Chem. Phys.* **88**, 6870 (1988).
- [35] A. Assion, T. Baumert, M. Bergt, T. Brixner, B. Kiefer, V. Seyfried, M. Strehle, and G. Gerber, *Science* **282**, 919 (1998).
- [36] D. Keefer and R. de Vivie-Riedle, *Acc. Chem. Res.* **51**, 2279 (2018).
- [37] K. L. Litvinenko, N. H. Le, B. Redlich, C. R. Pidgeon, N. V. Abrosimov, Y. Andreev, Z. Huang, and B. N. Murdin, *Nat. Commun.* **12**, 454 (2021).
- [38] Z. Chen, M. Shapiro, and P. Brumer, *J. Chem. Phys.* **102**, 5683 (1995).
- [39] M. Shapiro, Z. Chen, and P. Brumer, *Chem. Phys.* **217**, 325 (1997).
- [40] U. Fano, *Phys. Rev.* **124**, 1866 (1961).
- [41] D. Wehrli, M. Génévriez, C. Kreis, J. A. Agner, and F. Merkt, *J. Phys. Chem. A* **124**, 379 (2020).
- [42] K. J. R. Rosman and P. D. P. Taylor, *Pure Appl. Chem.* **70**, 217 (1998).
- [43] G. Herzberg, *Spectra of Diatomic Molecules*, 2nd ed., Molecular Spectra and Molecular Structure Vol. I (Van Nostrand Reinhold, New York, 1950).
- [44] B. W. Shore, *Theory of Coherent Atomic Excitation* (Wiley, New York, 1990), Vol. 44.
- [45] R. N. Zare, *Angular Momentum: Understanding Spatial Aspects in Chemistry and Physics* (Wiley, New York, 1988).
- [46] H. Lefebvre-Brion and R. W. Field, *The Spectra and Dynamics of Diatomic Molecules* (Elsevier, Amsterdam, 2004), pp. 347–467.
- [47] D. Bellert and W. H. Breckenridge, *Chem. Rev.* **102**, 1595 (2002).
- [48] M. Génévriez, D. Wehrli, and F. Merkt, *Phys. Rev. A* **100**, 032517 (2019).
- [49] J. Bezanson, A. Edelman, S. Karpinski, and V. B. Shah, *SIAM Rev.* **59**, 65 (2017).
- [50] H. Lefebvre-Brion and R. W. Field, *The Spectra and Dynamics of Diatomic Molecules* (Elsevier, Amsterdam, 2004), pp. 469–549.
- [51] P. Knight, M. Lauder, and B. Dalton, *Phys. Rep.* **190**, 1 (1990).
- [52] O. Faucher, E. Hertz, B. Lavorel, R. Chaux, T. Dreier, H. Berger, and D. Charalambidis, *J. Phys. B: At. Mol. Opt. Phys.* **32**, 4485 (1999).
- [53] D. Wehrli, M. Génévriez, and F. Merkt, *Phys. Rev. A* **100**, 012515 (2019).
- [54] T. F. Gallagher, *Rydberg Atoms* (Cambridge University Press, Cambridge, UK, 1994).
- [55] A. Kramida, Y. Ralchenko, and J. Reader, NIST Atomic Spectra Database (version 5.8), doi: [10.18434/T4W30F](https://doi.org/10.18434/T4W30F) (2020).
- [56] A. M. Gardner, C. D. Withers, J. B. Graneek, T. G. Wright, L. A. Viehland, and W. H. Breckenridge, *J. Phys. Chem. A* **114**, 7631 (2010).
- [57] R. S. Mulliken, *Phys. Rev.* **136**, A962 (1964).
- [58] R. S. Mulliken, *J. Chem. Phys.* **52**, 5170 (1970).
- [59] R. H. Lipson and R. W. Field, *J. Chem. Phys.* **110**, 10653 (1999).
- [60] E. Kleimenov, O. Zehnder, and F. Merkt, *J. Mol. Spectrosc.* **247**, 85 (2008).
- [61] R. J. Le Roy, *J. Quant. Spectrosc. Radiat. Transf.* **186**, 179 (2017).
- [62] C. Douketis, G. Scoles, S. Marchetti, M. Zen, and A. J. Thakkar, *J. Chem. Phys.* **76**, 3057 (1982).
- [63] C. Gaiser and B. Fellmuth, *Phys. Rev. Lett.* **120**, 123203 (2018).
- [64] J. M. Standard and P. R. Certain, *J. Chem. Phys.* **83**, 3002 (1985).
- [65] J. Mitroy and J. Y. Zhang, *Eur. Phys. J. D* **46**, 415 (2008).
- [66] O. Zehnder, R. Mastalerz, M. Reiher, F. Merkt, and R. A. Dressler, *J. Chem. Phys.* **128**, 234306 (2008).